Prediction of transient response for a 25-cm^2 PEM fuel cell

S. Shimpalee [a,*], D. Spuckler [b], J.W. Van Zee [a]

[a] *Department of Chemical Engineering, University of South Carolina, Columbia, SC 29208, USA*
[b] *CD-adapco, Seattle Office, 3150 Richards Rd. Suite #204, Bellevue, WA 98005, USA*

Abstract

A time dependence of three-dimensional simulation including water phase change and heat transfer of a PEMFC model has been studied. The overshoot behavior has been observed during a change in the electrical load during operation with fixed flow rates of hydrogen and air. The simulation of 25-cm^2 active area with a serpentine flow path shows the interactions of the anode and cathode flow streams, the flow through the gas diffusion media, and the movement of water through the MEA by electroosmotic and back diffusion forces. The simulation used a commercial computational fluid dynamics (CFD) solver, STAR-CD with and add-on PEMFC module, es-pemfc. The operating conditions corresponded to 101 kPa, 70 °C cell temperature, anode and cathode dew points and stoichiometries of 78 °C and 72 °C and 1.2 and 2.0 at an initial operating voltage of 0.7 V and current density of 0.57 A cm^{-2}.
© 2007 Elsevier B.V. All rights reserved.

1. Introduction

Proton exchange membrane fuel cells (PEMFCs) produce power for electric drive motors with less pollution. A full-scale three-dimensional solution to the time dependent Navier–Stokes equations for the flow channel and diffusion layers has been developed by including water phase change model [1,2] to improve the investigation of transient behavior of the fuel cell and its performance, which can be changed to meet the requirements of the amplitude and frequency of the load changes.

Many researchers have studied the problem of water management and distributions inside the PEM fuel cell especially under steady state operation as discussed in Wang [3] and Baschuk and Li [4]. Moreover, several groups [5–17] are improving their computational models to be more realistic, faster in computing, or to be able to be used for design improvement of PEMFC. Meng and Wang [8] improved their three-dimensional (3D) computational fluid dynamics (CFD) model to be more accurate to investigate two-phase behavior under different gas utilizations although the energy transport was ignored. Kulikovsky et al. [10] presented a simplified analytical model to obtain physical parameters and

then input those parameters into a quasi-3D model to speed up the PEMFC calculation. Oosthuizen et al. [13] used a 3D model to study the gas crossover between side-by-side channels under different flow rates, channel path length flow fields, and GDL porosities. Their results might be useful for flow field design improvements of the PEMFC. The multidimensional model calculations provide details inside the fuel cell on a local level and describe distributions of current, heat, and water. Thus, modeling will help in gaining an understanding of the mechanisms inside the fuel cell, aid in experimental data analysis, and identify limiting parameters.

The above mentioned modeling studies simulated a steady state operation of the fuel cell but a dynamic simulation is needed for PEMFC while operating conditions are changing, e.g. when the power required is changing under automotive application. Kim et al. [18–20] presented transient experimental results of 25-cm^2 active area PEMFC while the cell potential was varied with different rate. They also studied the effect of flow field design and fuel dilution on dynamic response of PEMFC. Their results indicate current overshoot behavior while the system requires more power rapidly and undershoot behavior while it requires less power. The peak of overshoot and undershoot current density depend on flow filed design, range of power change, gas component, and manifold configuration. Many experimentalists continue working on PEMFC research under dynamic

---

* Corresponding author. Tel.: +1 803 576 6140; fax: +1 803 777 8265.
E-mail address: shimpale@engr.sc.edu (S. Shimpalee).

Nomenclature

a_k	activity of water in stream k
A_{cv}	specific surface area of the control volume (c.v.) (m^{-1})
Area$_{cv}$	surface area of control volume (m^2)
C	condensation rate (s^{-1})
C_{wk}	concentration of water vapor at kth interface of the membrane (mol m^{-3})
C_{wlk}	concentration of water liquid at kth interface of the membrane (mol m^{-3})
D_h	hydraulic diameter of flow channel (m)
$D_{H_2,l}$	diffusion coefficient of H_2 in liquid water film (6.3E−9 $m^2\,s^{-1}$)
$D_{n,j}$	binary diffusion coefficient of species n in mixture j ($m^2\,s^{-1}$)
$D_{O_2,l}$	diffusion coefficient of O_2 in liquid water film (2.4E−9 $m^2\,s^{-1}$)
D_w	diffusion coefficient of water ($m^2\,s^{-1}$)
F	Faraday constant (96,487 C mole-of-electrons^{-1})
h_{fg}	enthalpy of vaporization for water (kJ kg^{-1})
$h_{formation}$	enthalpy of water formation (kJ $kmol^{-1}$)
$H_{H_2,l}$	Henry's law constant for hydrogen in liquid water film (8.9E−9 Pa)
$H_{O_2,l}$	Henry's law constant for oxygen in liquid water film (2.12E−10 Pa)
I	local current density (A m^{-2})
I_0	exchange current density (A m^{-2})
mass$_n$	mass of species n (kg)
$m_{n,k}$	mass fraction of the species n in stream k
m_{wl}	mass fraction of liquid water
$M_{m,dry}$	equivalent weight of a dry membrane (kg mol^{-1})
M_n	molecular weight of species n (kg mol^{-1})
n_d	electro-osmotic drag coefficient (number of water molecules carried per proton)
P	pressure (Pa)
P_n	partial pressure of species n (Pa)
$P_{w,k}^{sat}$	vapor pressure of water in stream k (Pa)
Q	volume flow rate ($m^3\,s^{-1}$)
R	universal gas constant (8.314 J $mol^{-1}\,K^{-1}$)
S	source term
t	time (s)
$t_{f,a}$	liquid water film on the anode (m)
$t_{f,c}$	liquid water film on the cathode (m)
t_m	membrane thickness (m)
T	temperature (K)
$u,\ v,\ w$	velocities in x, y, and z directions, respectively ($m\,s^{-1}$)
V_{oc}	cell open-circuit voltage (V)
V_{cell}	cell voltage (V)
x	channel length measured from anode inlet (m)
X_n	mole fraction of species n
$X_{w,k}$	mole fraction of water in stream k

Greek symbols

α	net water flux per proton flux
α_a	anode transfer coefficient
α_c	cathode transfer coefficient
β_ξ	permeability in the ξ direction
ε	porosity of gas diffusion layer
η	over potential for oxygen reaction (V)
λ	water content in the membrane
μ	dynamic viscosity (kg $s^{-1}\,m^{-2}$)
ρ	density of the mixture (kg m^{-3})
$\rho_{m,dry}$	density of a dry membrane (kg m^{-3})
σ_m	membrane conductivity ($\Omega^{-1}\,m^{-1}$)

Subscripts and superscripts

a	anode
c	cathode
e	electrochemical reaction
H_2	hydrogen
K	anode or cathode
l	liquid
N_2	nitrogen
O_2	oxygen
p	phase change
sat	saturated
v	vapor
w	water
ξ	dummy variable for direction x, y, or z

response including stack design, contaminants, flow-field, etc. For example, Hamelin et al. [21] revealed three different transient responses on Ballard fuel cell stack model MK5-E, which has maximum output of 10 kW. Amphlett et al. [22] gave the experimental results of a hybrid PEMFC/battery system. They showed how their hybrid system and components interacted during charging or discharging. Mohtadi et al. [23] showed dynamic response of current density when PEMFC was exposed by H_2S while analyzing the effect of temperature on the adsorption rate of H_2S on Pt anodes. Emonts et al. [24] studied the dynamics of a PEMFC, a compact methanol reformer, and the choice of a short-term storage system for an automotive application. Only few research groups have included transient simulation of PEMFCs in their studies. For instance, Wang and Wang [25] presented dynamics study on PEMFC using commercial CFD code. Their geometry was single straight channel flow-field that is not normally used in fuel cell application. Therefore, the effect of pressure driven flow underneath the gas diffusion layers has been ignored. Shimpalee et al. [26,27] showed numerical solutions of transient response of 10-cm^2 serpentine flow-field PEMFC under both excess and starve fuel/air. They concluded that the peak of overshoot depends on the rate of voltage change and utilization of reactants. The overshoot behavior is a result of local non-uniformity in distributions. However, their model did not take into account of temperature effect and phase change of water. Therefore, their results might be over predicted.
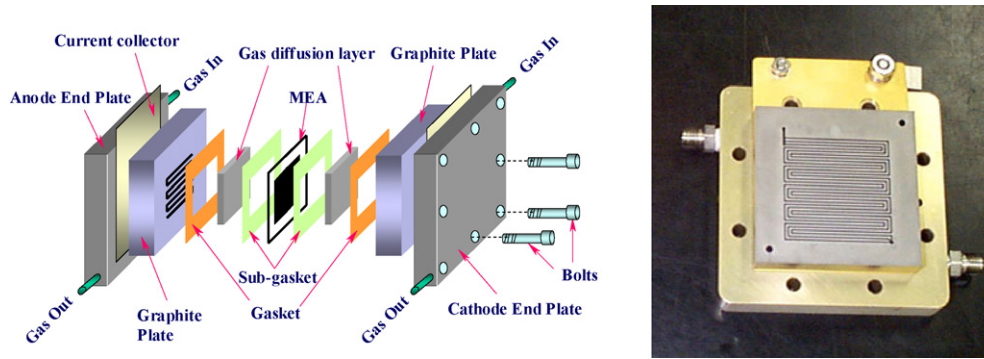
Fig. 1. The picture shows schematic of fuel cell assemble and actual flow-field plate with gas channel of 25-cm^2 PEMFC. There are 30 straight channels connected in a triple pass serpentine fashion. Anode side and cathode side flow channels are symmetric and placed property aligned (non-staggered) on top of each other.

In this study, the three-dimensional model of PEMFC with 25-cm^2 reacting area as shown in Fig. 1 was developed with the inclusion of time dependent analysis. The transient model of Shimpalee et al. [26,27] was used with the extension of energy and water phase change equations. Different rates of voltage change were chosen to study their effects on the PEM fuel cell performance at each time interval. Moreover, the detail of local current density, water distribution, and reactant concentration are investigated and compared with previous works [26,27].

2. Numerical procedure

Fig. 2 shows model geometry that created from Fig. 1. It has triple pass channel with 11 serpentine fashions. The geometry of fuel cell arrangement modeled in this work consists of two flow channels separated by diffusion layers and the membrane electrode assembly (MEA). Between diffusion layers and MEA, there are sub-gaskets. Therefore the active area of MEA is reduced from 25-cm^2 to 20-cm^2 as shown in Fig. 2b. There are triple pass channel with eleven serpentine passes in the flow path, so that the flow is approximately 55 cm long in the axial direction with 0.1 cm (height) × 0.08 cm (width) cross-section flow area in each channel. Each diffusion layer has dimensions of 0.025 cm (height) × 5.00 cm (width) × 5.00 cm (length). A total of 734,940 cells (elements) were used to model the fuel cell.

The equations used in this work are shown in Tables 1 and 2. These time dependent equations have been extended from Shimpalee et al. [26,27] to include the energy equation, and a water phase change model, where homogeneous two phase flow was assumed. In the water phase change model, when the local activity of water exceeded 1.0, water vapor was condensed to form liquid water until the local activity equaled 1.0. Conversely, if liquid water was present and the local activity of water dropped below 1.0, then liquid water was evaporated until the local activity equaled 1.0. When liquid water condensed in the region adjacent to the electrode surface, it is assumed to form a liquid film on the electrode surface. In the regions where there was a liquid film on the electrode, hydrogen and oxygen were required to dissolve in the liquid film and diffuse through the film to the electrode surface in order to react. Henry's law was used to calculate the solubility of the gases in the liquid. The thickness of this liquid film depends on the rate of condensa-

tion/evaporation and the production of water by electrochemical reaction as discussed in the appendix of Lee et al. [5] and Shimpalee and Van Zee [2]. Note that since the solubility of O$_2$ in the liquid film is low, the solution procedure includes transient calculation (see X$_{O_2}(x, y, z, t)$ in Eq. (30)) in the water film on the catalyst surface. This transient concentration and water film thickness corresponds to a lost in available surface reaction area when the film is thick or three phase boundary.

A control volume technique based on a commercial flow solver, STAR-CD 3.26, was used to solve the coupled governing equations [28] with transient analysis. This software was used with an add-on tool called Expert System for PEMFCs (es-pemfc version 2.20) that provided the source terms for the species transport equations, the phase change equations for water, and the heat
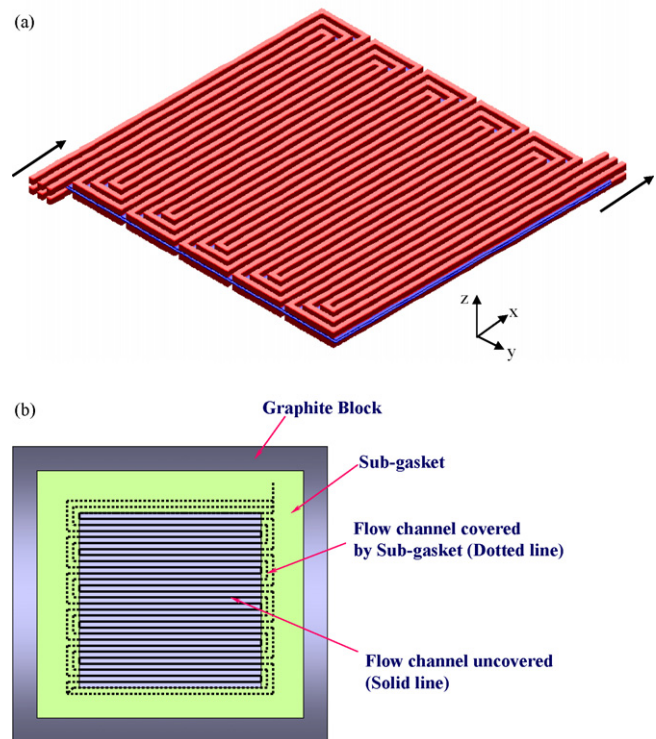

Fig. 2. (a) The geometrical model of the complete 25-cm^2 fuel cell shown without graphite current collector. There are 33 straight channels connected in a triple pass serpentine fashion shown in Fig. 1. (b) Schematics of sub-gasket and flow channel (20-cm^2 active area due to sub-gasket).

Table 1
(a) Governing equations and (b) source terms for governing equation in (a)

Governing equations	Mathematical expressions	
(a)		
Conservation of mass	$\frac{\partial \rho}{\partial t} + \frac{\partial(\rho u)}{\partial x} + \frac{\partial(\rho v)}{\partial y} + \frac{\partial(\rho w)}{\partial z} = S_m$	(2)
Momentum transport	$\frac{\partial \rho u}{\partial t} + u\frac{\partial(\rho u)}{\partial x} + v\frac{\partial(\rho u)}{\partial y} + w\frac{\partial(\rho u)}{\partial z} = -\frac{\partial P}{\partial x} + \frac{\partial}{\partial x}\left(\mu\frac{\partial u}{\partial x}\right) + \frac{\partial}{\partial y}\left(\mu\frac{\partial u}{\partial y}\right) + \frac{\partial}{\partial z}\left(\mu\frac{\partial u}{\partial z}\right) + S_{px}$ $\frac{\partial \rho v}{\partial t} + u\frac{\partial(\rho v)}{\partial x} + v\frac{\partial(\rho v)}{\partial y} + w\frac{\partial(\rho v)}{\partial z} = -\frac{\partial P}{\partial y} + \frac{\partial}{\partial x}\left(\mu\frac{\partial v}{\partial x}\right) + \frac{\partial}{\partial y}\left(\mu\frac{\partial v}{\partial y}\right) + \frac{\partial}{\partial z}\left(\mu\frac{\partial v}{\partial z}\right) + S_{py}$ $\frac{\partial \rho w}{\partial t} + u\frac{\partial(\rho w)}{\partial x} + v\frac{\partial(\rho w)}{\partial y} + w\frac{\partial(\rho w)}{\partial z} = -\frac{\partial P}{\partial z} + \frac{\partial}{\partial x}\left(\mu\frac{\partial w}{\partial x}\right) + \frac{\partial}{\partial y}\left(\mu\frac{\partial w}{\partial y}\right) + \frac{\partial}{\partial z}\left(\mu\frac{\partial w}{\partial z}\right) + S_{pz}$	(3)
Hydrogen transport (anode side)	$\frac{\partial \rho m_{H_2}}{\partial t} + u\frac{\partial(\rho m_{H_2})}{\partial x} + v\frac{\partial(\rho m_{H_2})}{\partial y} + w\frac{\partial(\rho m_{H_2})}{\partial z} = \frac{\partial(J_{x,H_2})}{\partial x} + \frac{\partial(J_{y,H_2})}{\partial y} + \frac{\partial(J_{z,H_2})}{\partial z} + S_{H_2}$	(4)
Water vapor transport	$\frac{\partial \rho m_{wv}}{\partial t} + u\frac{\partial(\rho m_{wv})}{\partial x} + v\frac{\partial(\rho m_{wv})}{\partial y} + w\frac{\partial(\rho m_{wv})}{\partial z} = \frac{\partial(J_{x,wv})}{\partial x} + \frac{\partial(J_{y,wv})}{\partial y} + \frac{\partial(J_{z,wv})}{\partial z} + S_{wv_p} + S_{awv_e} + S_{cwv_e}$	(5)
Water liquid transport	$\frac{\partial \rho m_{wl}}{\partial t} + u\frac{\partial(\rho m_{wl})}{\partial x} + v\frac{\partial(\rho m_{wl})}{\partial y} + w\frac{\partial(\rho m_{wl})}{\partial z} = \frac{\partial(J_{x,wl})}{\partial x} + \frac{\partial(J_{y,wl})}{\partial y} + \frac{\partial(J_{z,wl})}{\partial z} + S_{wl_p}$	(6)
Oxygen transport (cathode side)	$\frac{\partial \rho m_{O_2}}{\partial t} + u\frac{\partial(\rho m_{O_2})}{\partial x} + v\frac{\partial(\rho m_{O_2})}{\partial y} + w\frac{\partial(\rho m_{O_2})}{\partial z} = \frac{\partial(J_{x,O_2})}{\partial x} + \frac{\partial(J_{y,O_2})}{\partial y} + \frac{\partial(J_{z,O_2})}{\partial z} + S_{O_2}$	(7)
Energy equation	$\frac{\partial \rho h}{\partial t} + \frac{\partial(\rho u h)}{\partial x} + \frac{\partial(\rho v h)}{\partial y} + \frac{\partial(\rho w h)}{\partial z} = \frac{\partial}{\partial x}\left(k\frac{\partial T}{\partial x}\right) + \frac{\partial}{\partial y}\left(k\frac{\partial T}{\partial y}\right) + \frac{\partial}{\partial z}\left(k\frac{\partial T}{\partial z}\right) + S_{h_p} + S_{h_e}$	(8)
	Non-zero volumetric source terms	
(b)		
Conservation of mass	$S_m = S_{H_2} + S_{wv_p} + S_{wl_p} + S_{wv_e}$ at anode GDL/MEA interface $S_m = S_{O_2} + S_{wv_p} + S_{wl_p} + S_{wv_e}$ at cathode GDL/MEA interface	(9)
Momentum transport	$S_{px} = -\frac{\mu u}{\beta_x}, \quad S_{py} = -\frac{\mu v}{\beta_y}, \quad S_{pz} = -\frac{\mu w}{\beta_z}$ at GDLs	(10)
Hydrogen transport (anode side)	$S_{H_2} = -\frac{I(x,y,t)}{2F}M_{H_2}A_{cv}$ at anode GDL/MEA interface	(11)
Water vapor transport	$S_{wv_p} = \frac{M_{H_2O}\sum_{n\,of\,v}\text{mass}_{n\,of\,v}(x,y,z,t)/M_{n\,of\,v}}{1-(P_{wv}^{sat}(T,t)/P(x,y,z,t))}\left[\frac{P_{wv}^{sat}(T,t) - P_{wv}(x,y,z,t)}{P(x,y,z,t)}\right] * r$ at entire fluid domain	(12)
	$S_{awv_e} = -\frac{\alpha(x,y,t)}{F}I(x,y,t)M_{H_2O}A_{cv}$ at anode GDL/MEA interface	(13)
	$S_{cwv_e} = \frac{1+2\alpha(x,y,t)}{2F}I(x,y,t)M_{H_2O}A_{cv}$ at cathode GDL/MEA interface	(14)
Water liquid transport	$S_{wl_p} = -S_{wv_p}$ at entire fluid domain	(15)
Oxygen transport (cathode side)	$S_{O_2} = -\frac{I(x,y,t)}{4F}M_{O_2}A_{cv}$ at cathode GDL/MEA interface	(16)
Energy equation	Heat source by energy losses: $S_{h_e} = h_{formation} * \left[\frac{1}{2F}I(x,y,t)*A_{cv}\right] - (I(x,y,t)V_{cell}A_{cv})$ at cathode GDL/MEA interface	(17)
	Heat source by phase change: $S_{h_p} = S_{wl_p} * h_{fg}$ at entire fluid domain	(18)

generation equations [2,29]. Also, es-pemfc accounted for the flux of protons and water across the membrane [2,29]. The material properties and operating conditions of this work are shown in Table 3. The transient load profile consists of changing the cell voltage from 0.7 V at steady state to 0.5 V with the rate of 1.0 V s^{-1} as shown in Table 4.

The transient solution procedure used in the STAR-CD flow solver is based on a PISO algorithm [28] where a predictor-corrector strategy is used. For each time step, a predictor, followed by a number of correctors, iteratively solves the linear equation sets for each main dependent variable. The mixture properties at each control volume are calculated based on the local species concentrations. The anode side gas mixture contains hydrogen and water. And, the cathode side gas mixture contains oxygen, water, and nitrogen. Therefore, the density and viscosity of the two flow channels are different and they vary from at each location and the newly calculated values of the variables prevail throughout the time step Δt.

3. Results and discussion

Fig. 3 shows how the averaged current density changes when the cell voltages are changed from 0.7 V to 0.5 V using transient load profile from Table 2. This figure indicates overshoot behavior. The averaged current density increases from 0.57 A cm^{-2} to 1.23 A cm^{-2} when the cell voltage is 0.52 V at time = 0.23 s and then the current density slowly decreases and reaches 1.15 A cm^{-2} at time = 0.35 s. The height of the overshoot can be changed by the rate of cell voltage change and by the flow rates as already discussed by our previous work [26] for the case of excess stoichiometry but here we fix the rate of voltage change and flow rate and study the dependent variables in order to understand their interactions during current overshoot behavior.

Fig. 4 shows the local current density distributions on the membrane surface at four different time steps and cell voltages. At the steady state current density of 0.57 A cm^{-2} correspond-

Table 2
Constitutive equation for modeling electrochemical effects

Diffusion mass flux of species n in ξ direction	$J_{\xi,n} = -\rho D_{\xi,n} \dfrac{\partial m_{K,n}}{\partial \xi}$	(19)
Net water transfer coefficient per proton	$\alpha(x,y,t) = n_d(x,y,t) - \dfrac{F}{I(x,y,t)} D_w(x,y,t) \dfrac{(C_{wc}(x,y,t) - C_{wa}(x,y,t))}{t_m}$	(20)
Water content in the membrane	$\lambda = 0.043 + 17.81a_a - 39.85a_a^2 + 36.0a_a^3; 0 < a_a \leq 1 = 14 + 1.4(a_a - 1); 1 < a_a \leq 3$	(21)
Electro-osmotic drag coefficient	$n_d(x,y,t) = 0.0029\lambda^2 + 0.05\lambda - 3.4 \times 10^{-19}$	(22)
Water diffusion coefficient	$D_w(x,y,t) = D_\lambda \exp\left(2416\left(\dfrac{1}{303} - \dfrac{1}{T(x,y,t)}\right)\right); D_\lambda = 10^{-10}, \lambda < 2; D_\lambda = 10^{-10}(1 + 2(\lambda - 2)), 2 \leq \lambda \leq 3; D_\lambda = 10^{-10}(3 - 1.67(\lambda - 3)), 3 < \lambda < 4.5; D_\lambda = 1.25 \times 10^{-10}, \lambda \geq 4.5$	(23)
Water vapor concentration for anode and cathode surfaces of the MEA	$C_{wK}(x,y,t) = \dfrac{\rho_{m,dry}}{M_{m,dry}}(0.043 + 17.8a_K - 39.8a_K^2 + 36.0a_K^3); a_K \leq 1 = \dfrac{\rho_{m,dry}}{M_{m,dry}}(14 + 1.4(a_K - 1));$ for $a_K > 1$, where $K = a$ or c	(24)
Water activity	$a_K = \dfrac{X_{w,K}(x,y,z,t)P(x,y,z,t)}{P_{w,K}^{sat}(T,t)}$	(25)
Local current density	$I(x,y,t) = \dfrac{\sigma_m(x,y,t)}{t_m}\{V_{oc} - V_{cell} - \eta(x,y,t)\}$	(26)
Local membrane conductivity	$\sigma_m(x,y,t) = \left(0.00514 \dfrac{M_{m,dry}}{\rho_{m,dry}} C_{wa}(x,y,t) - 0.00326\right)\exp\left(1268\left(\dfrac{1}{303} - \dfrac{1}{T(x,y,t)}\right)\right) \times 10^2$	(27)
Local over potential	$\eta(x,y,t) = \dfrac{RT(x,y,\text{cathode\_GDL/MEA},t)}{\alpha_c F} \ln\left[\dfrac{I(x,y,t)P(x,y,\text{cathode\_GDL/MEA},t)}{I_{0_{O_2}} P_{O_2}(x,y,\text{cathode\_GDL/MEA},t)}\right] + \dfrac{RT(x,y,\text{cathode\_GDL/MEA},t)}{\alpha_a F} \ln\left[\dfrac{I(x,y,t)P(x,y,\text{anode\_GDL/MEA},t)}{I_{0_{H_2}} P_{H_2}(x,y,\text{anode\_GDL/MEA},t)}\right]$	(28)
Water film thickness	$t_{f,k} = \dfrac{m_{wl}(\sum \text{mass}_n)}{\varepsilon \rho_{wl}\text{Area}_{cv}}$	(29)
Gas solubility	$P_{O_2}(x,y,z,t) = X_{O_2}(x,y,z,t)P(x,y,z,t)$ at cathode GDL/MEA interface	(30)
	$-\dfrac{I(x,y,t)}{4F} M_{O_2} = \rho m_{O_2} D_{O_2,l}\left[\dfrac{X_{O_2}(x,y,z - t_{f,c},t)P(x,y,z - t_{f,c},t)H_{O_2,l}^{-1} - X_{O_2}(x,y,z,t)}{t_{f,c}}\right]$ where $z =$ cathode GDL/MEA interface	(31)
	$P_{H_2}(x,y,z,t) = X_{H_2}(x,y,z,t)P(x,y,z,t)$ at anode GDL/MEA interface	(32)
	$-\dfrac{I(x,y,t)}{2F} M_{H_2} = \rho m_{H_2} D_{H_2,l}\left[\dfrac{X_{H_2}(x,y,z + t_{f,a},t)P(x,y,z + t_{f,a},t)H_{H_2,l}^{-1} - X_{H_2}(x,y,z,t)}{t_{f,a}}\right]$ where $z =$ anode GDL/MEA interface	(33)

Table 3
Material properties and operating condition at 0.7 V corresponding to stoichiometry of 1.2/2.0 at $0.57\,\text{A}\,\text{cm}^{-2}$

Anode channel inlet conditions	Velocity (m s^{-1})	2.23
	Mole fraction of H$_2$	0.53
	Mole fraction of H$_2$O	0.47
	Dew-point temperature (°C)	78
Cathode channel inlet conditions	Velocity (m s^{-1})	6.8
	Mole fraction of O$_2$	0.14
	Mole fraction of N$_2$	0.50
	Mole fraction of H$_2$O	0.36
	Dew-point temperature (°C)	72
Operating conditions	Cell temperature (°C)	70
	Operating pressure (kPa)	101
Current collector	Thermal conductivity (W m^{-1} K^{-1})	5.7
GDLs	Thickness after compressed (μm)	250
	Permeability (m^2)	3.3E−15
	Porosity after compressed (%)	70
	Diffusion adjustment (%)	50
	Thermal conductivity (W m^{-1} K^{-1})	0.21
Membrane	Gore PRIMEA®5561	

ing to the cell voltage of 0.7 V and $t = 0.10$ s, the local current density is higher at the inlet region and decreasing along the flow channel towards the outlet due to the consumption of reactants and the reduction of anode water activity. The maximum and minimum local densities are $\sim 0.60\,\text{A}\,\text{cm}^{-2}$ and $\sim 0.50\,\text{A}\,\text{cm}^{-2}$,
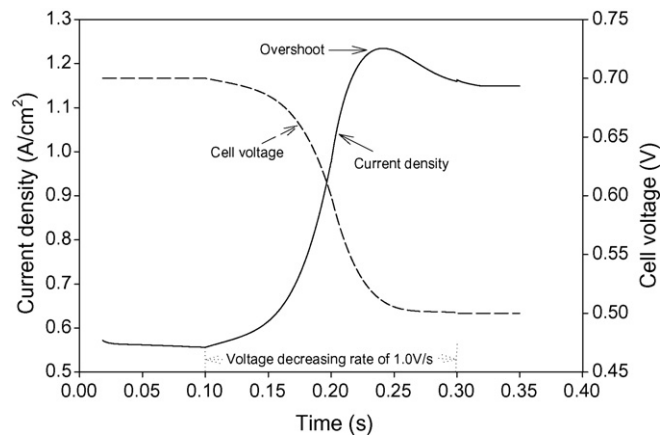

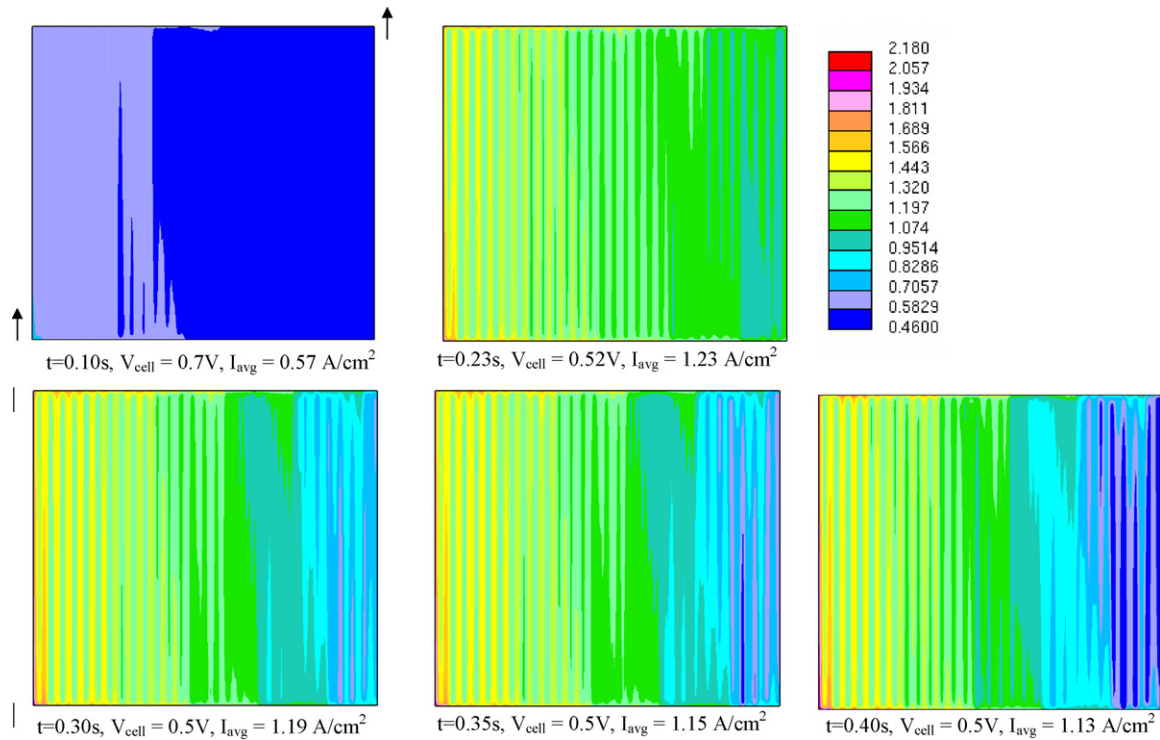Fig. 3. Average current density for change from 0.7 V to 0.5 V.

Fig. 4. Local transient current density (A cm^{-2}) contours on MEA surface at different times and cell voltages.

respectively, which represents small variation over the entire active cell area. When the cell voltage is dropped to 0.52 V at time = 0.23 s, the local current density significantly increases over the membrane surface however, the contour pattern is similar to when cell voltage is 0.7 V. The highest local current density is ~2.18 A cm^{-2} and the lowest value is ~0.95 A cm^{-2}. When the time increases to 0.30 s and the cell voltage is 0.5 V, there is more non-uniformity of local current density distribution. The local current reduces considerably on the MEA region from the center of membrane surface toward the outlet due to strong decreasing of oxygen concentration. The highest local current density is located around the inlet with a value of 2.0 A cm^{-2} and the lowest local current density is at the outlet with a value of 0.58 A cm^{-2}. When PEMFC performance reaches steady state at cell voltage of 0.5 V and time is greater than 0.35 V, the decreasing of local current density from the center region of the membrane surface towards the outlet region is more significant. The current density in this case varies from 2.0 A cm^{-2} to 0.46 A cm^{-2}, which represents considerable variations along the membrane surface. For the case under consideration, at steady state cell voltage of 0.5 V, the local current density does not significantly vary over the first half of the membrane surface, but it sharply decreases over the second half of membrane surface. This is because the high reaction rate regions (i.e., first half of the membrane surface) accompany excessive hydrogen and oxygen consumptions and therefore they depleted in these regions (i.e., second half of the membrane surface).

To further describe the overshoot phenomena, the profile plots across MEA width and serpentine flow path at $x = 2.5$ cm as shown in Fig. 5 are examined. Fig. 6 shows the transient profiles of local oxygen mole fraction across the MEA width and channel

as shown in Fig. 5. At cell voltage of 0.7 V and steady state, the oxygen mole fraction decreases along the electrode width from inlet toward the outlet due to its consumption from electrochemical reaction, which is consistent with the local current density distribution from Fig. 4. When cell voltage is reducing to 0.58 V at time = 0.2 s, its distribution shows more non-uniform due to the higher reduction of oxygen concentration by higher reaction rate. The much more non-uniform distribution of oxygen mole fraction is revealed at cell voltage of 0.52 V at time = 0.23 s, especially in the first half of the cell where the reaction rate
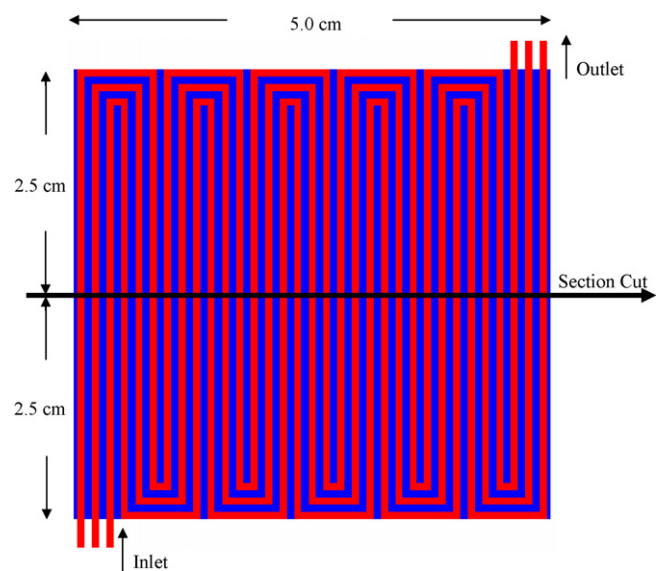

Fig. 5. Top view projection of serpentine flow-field showing location of analysis.

Table 4
Cell voltage changes from 0.7 V to 0.5 V in 0.2 s

Time (s)	0.10	0.125	0.15	0.17	0.18	0.19	0.20	0.21	0.23	0.24	0.26	0.28	0.30
Cell voltage (V)	0.70	0.695	0.685	0.67	0.65	0.63	0.60	0.57	0.52	0.51	0.505	0.5025	0.50
Predicted current density (A cm^{-2})	0.56	0.58	0.62	0.69	0.76	0.85	0.98	1.11	1.23	1.22	1.21	1.18	1.15
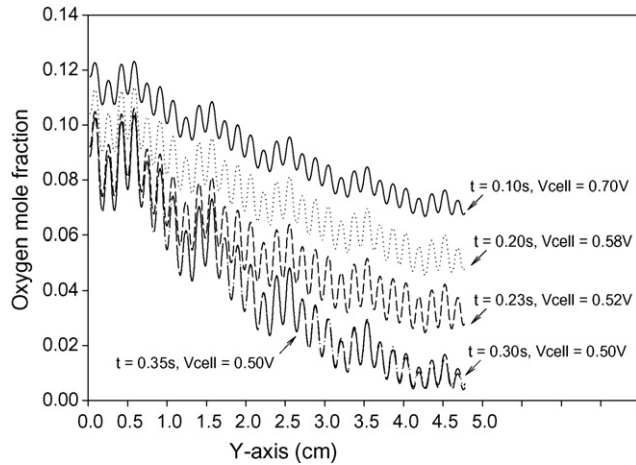
Fig. 6. Variation of oxygen mole fraction along channel width at different times and cell voltages.

is higher and it has much lower concentration in the second half of the cell. Again at this time, the PEMFC gives the maximum average current density. When the cell voltage is reaching 0.5 V after time greater than 0.23 s, the oxygen concentration is depleting in the second half of the cell (i.e., a mole fraction between 0.02 and 0.005) and this limits the current density in these locations. Therefore, the current density becomes decreasing thus indicating overshoot behavior. When cell voltage of 0.5 V reaches steady state performance, the slope of oxygen mole fraction profile becomes negatively steeper in the first half of the cell and remains minimal value in the second half of the cell. In summary, when the cell voltage is decreasing, the rate of gas consumption is increasing and the oxygen concentration decreases.
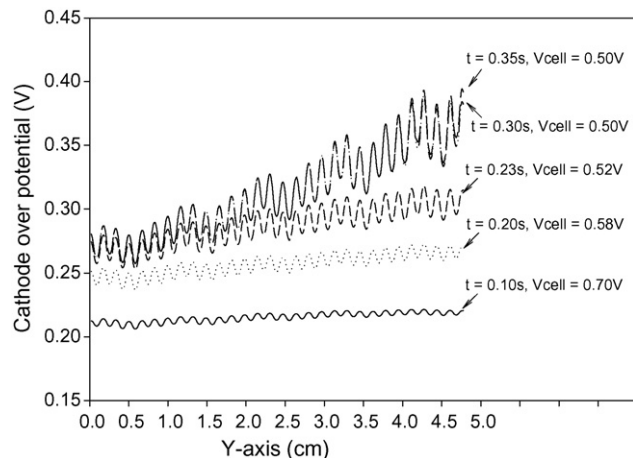
Fig. 7 presents transient response of cathode over potential or cathode polarization that is a function of partial pressure of oxygen. As already indicated in Fig. 6 as oxygen mole fraction response with time and cell voltage change, those profiles affect cathode kinetic significantly. At time = 0.1 s and cell voltage is 0.7 V, there is not significant polarization at cathode surface because there is plenty of oxygen available in the PEMFC as shown in Fig. 6. When current is increasing and reaches the peak overshoot (cell voltage = 0.52 V and time is 0.23 s), cathode over potential or polarization increases with about the same slope or rate along electrode width (Y-axis) as the initial point of 0.7 V. This is because the consumption of oxygen is increasing but its concentration has not depleted. After $t = 0.23$ s and the cell voltage is remaining constant at 0.5 V with constant flow rate of reactants, the cathode polarization is increasing especially at Y-axis is greater than 2.5 cm (second half of MEA surface), which is consistent with the depletion of oxygen concentration as discusses in Fig. 6. This profile reaches steady state of $V_{cell} = 0.5$ V at $t = 0.35$ s. This will drop performance or current density thus indicating overshoot phenomenon.

Fig. 8 shows transient response of liquid water film thickness profiles along the MEA width at the cathode side. This figure shows that the liquid water film is increasing from inlet toward outlet due to the production of water vapor by electrochemical reaction and then water vapor can be condensed to liquid water if water activity is greater than 1.0. This figure also shows the accumulation of liquid water from time = 0.10 s at 0.7 V to time = 0.35 at 0.5 V. This accumulation of liquid water could decrease the PEMFC performance by creating the high gases resistance known as water flooding. However in this condition, the liquid water presented in this system seems to be insignificantly to decrease the PEMFC performance.

Fig. 7. Variation of cathode over potential (V) along channel width at different times and cell voltages.
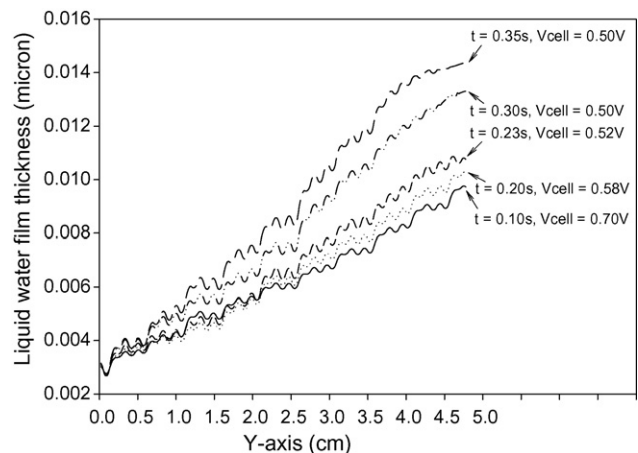

Fig. 8. Variation of liquid water film thickness (micron) along the centerline on cathode electrode at different times and cell voltages.
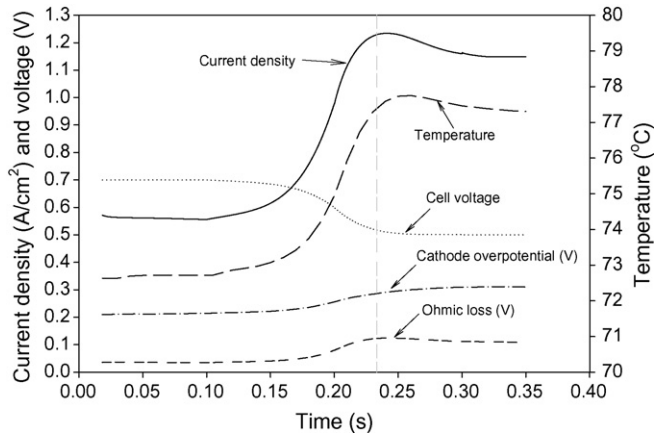
Fig. 9. Average cell current, cathode over potential, ohmic loss, and temperature response during a transient load change.

Fig. 10. Comparison of transient behaviors between single phase, isothermal model and water phase change, non-isothermal model.

Fig. 9 presents the transient average temperature on the anode MEA surface, cathode over potential, and ohmic loss correspond to particular average current density and the cell voltage at each time step. This results shows that temperature increases when the cell voltage is decreased. This is because the reduction of cell voltage escalates the reaction rate thus increasing heat generation caused by electrochemical reaction. Note that the increase in temperature results in lower membrane water content, thus dropping in ionic conductivity. Further, the rate of temperature rise is much slower than the rate of current density change. Therefore, the overshoot in temperature is not as significant as the current density overshoot in this study. For the cathode over potential profile, it increases when the current density is increasing, which is similar to the ohmic potential profile. However, after the current density reaches the peak of overshoot, cathode over potential continues increasing due to the loss of oxygen concentration near the exit region as explained earlier. Consequently, current density starts to decrease, thus causing the lower temperature. Meanwhile, the ohmic loss is slightly decreasing due to the increasing in membrane water content because of the lower temperature. Therefore, the contribution of ohmic loss or membrane conductivity and temperature in this particular operating condition could be the controlling factor in the peak and magnitude of overshoot.

Fig. 10 presents the comparison of transient behavior between the transient current results of single phase isothermal model [27] on 10-cm^2 active area and phase change model on 25-cm^2 active area. For better comparison, the current densities shown in this figure need to be dimensionless with average current density of each time step ($I(t)$) is divided by average steady state current density at cell voltage of 0.5 V ($I_{steady\ state\ at\ 0.5\ V}$) as equation presented below.

$$I(t) = \frac{I(t)}{I_{steady\ state\ at\ 0.5\ V}} \qquad (1)$$

The result reveals that the current density of single phase, isothermal model has much higher overshoot than the result of water phase change, non-isothermal model. Moreover the rate of current density reduction after overshoot point of single phase, isothermal model is faster than phase change model. This could
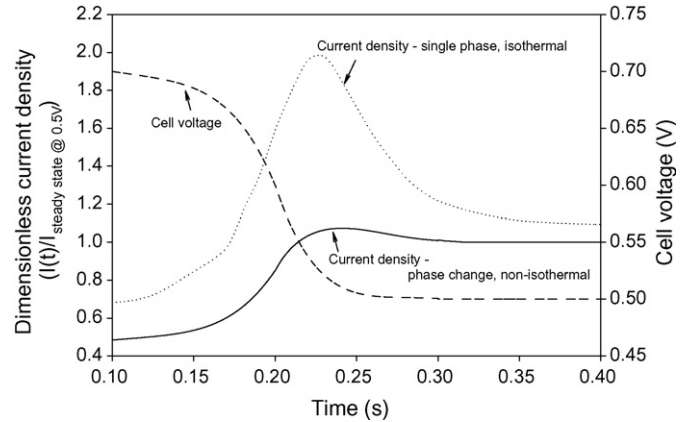
be the effect of temperature and water phase change that included into this recent model.

4. Conclusions

A three-dimensional including water phase change and energy balance with transient simulation of PEM fuel cell was studied at fixed flow rates of feed gases. The flow rates correspond to normal fuel and oxygen utilization (1.2/2.0 stoich) at the high cell voltage and a minimal operating condition at the low cell voltage. The cell voltage was changed from 0.7 V to 0.5 V at a somewhat rapid rate of 1.0 V s^{-1} and overshoot behavior in the current was observed and explained in terms of the distributions of current density, oxygen concentration, liquid water, and temperature.

When the cell voltage is decreased, the current density increases and reaches the peak of overshoot while the capacity of the reactants in the flow channels is used. This steady state values correspond to a highly non-uniform local current density distribution, dependent on local concentrations of the reacting gases. For this condition, oxygen appears to control the distribution. Single phase and isothermal model shows higher overshoot than water phase change and non-isothermal model because temperature rise affects the peak of overshoot. Therefore, water phase change and non-isothermal effects are important in a transient PEMFC model. Moreover, the controlling mechanism of overshoot is dependent on the gases utilizations and the rate of load change. These results may help effort in the design of the flowfield and manifold configuration. These design changes may improve stack performance.

References

[1] S. Shimpalee, S. Dutta, Numerical Heat Transfer, Part A 38 (2000) 111–128.

[2] S. Shimpalee, J.W. Van Zee, Int. J. Hydrogen Energy, doi:10.1016/j.ijhydene.2006.11.032, in press.

[3] C.Y. Wang, Chem. Rev. 104 (2004) 4727–4766.

[4] J.J. Baschuk, X. Li, J. Power Sources 142 (2004) 134–153.

[5] W.-K. Lee, S. Shimpalee, J.W. Van Zee, J. Electrochem. Soc. 150 (2003) A341–A348.

[6] T. Zhou, H. Liu, J. Power Sources 138 (2004) 101–110.

[7] S. Shimpalee, S. Greenway, D. Spuckler, J.W. Van Zee, J. Power Sources 135 (2004) 79–87.

[8] H. Meng, C.Y. Wang, J. Electrochem. Soc. 152 (9) (2005) A1733–A1741.

[9] J.G. Pharoah, J. Power Sources 144 (2005) 77–82.

[10] A.A. Kulikovsky, T. Wüster, A. Egman, D. Stolten, J. Electrochem. Soc. 152 (6) (2005) A1290–A1300.

[11] W. Ying, Y.-J. Sohn, W.-Y. Lee, J. Ke, C.-S. Kim, J. Power Sources 145 (2005) 563–571.

[12] B.R. Sivertsen, N. Djilali, J. Power Sources 141 (2005) 65–78.

[13] P.H. Oosthuizen, L. Sun, K.B. McAuley, Appl. Therm. Eng. 25 (2005) 1083–1096.

[14] H. Meng, C.Y. Wang, J. Fuel Cells 5 (4) (2005) 455–462.

[15] S. Litster, J.G. Pharoah, G. McLean, N. Djilali, J. Power Sources 156 (2) (2006) 334–344.

[16] P.P. Mukherjee, C.Y. Wang, J. Electrochem. Soc. 153 (5) (2006) A840–A849.

[17] X.L. Liu, W.Q. Tao, Z.Y. Li, Y.L. He, J. Power Sources 158 (1) (2006) 25–35.

[18] S.-H. Kim, S. Shimpalee, J.W. Van Zee, J. Electrochem. Soc. 152 (2005) A1265–A1271.

[19] S.-H. Kim, S. Shimpalee, J.W. Van Zee, J. Power Sources 137 (2004) 43–52.

[20] S.-H. Kim, S. Shimpalee, J.W. Van Zee, J. Power Sources 135 (2004) 110–121.

[21] J. Hamelin, K. Agbossou, A. Laperriere, F. Laurencelle, T.K. Bose, Int. J. Hydrogen Energy 26 (2001) 625–629.

[22] J.C. Amphlett, E.H. De Oliveria, R.F. Mann, P.R. Roberge, A. Rodrigues, J.P. Salvador, J. Power Sources 65 (1997) 173–178.

[23] R. Mohtadi, W.-K. Lee, J.W. Van Zee, J. Appl. Catal. B: Environ. 56 (2005) 37–42.

[24] B. Emonts, J. Bogild Hansen, H. Schmidt, T. Grube, B. Hohlein, R. Peters, A. Tschauder, J. Power Sources 86 (2000) 228–236.

[25] Y. Wang, C.Y. Wang, Electrochim. Acta 50 (2005) 1307–1315.

[26] S. Shimpalee, W.-K. Lee, J.W. Van Zee, H. Naseri-Neshat, J. Power Sources 156 (2006) 355–368.

[27] S. Shimpalee, W.-K. Lee, J.W. Van Zee, H. Naseri-Neshat, J. Power Sources 156 (2006) 369–374.

[28] Star-CD 3.2 Methodology, CD adapco Group, http://www.adapco.com.

[29] ES-PEMFC Methodology and Tutorial Manual, CD adapco Group, http://www.adapco.com.